Numerical Investigation of Ice Crystal Impact Characteristics in Compressor Cascade

JIA Wei[1*], *GU Yuanhao*[2]

1. College of Safety Science and Engineering, Civil Aviation University of China, Tianjin 300300, P. R. China;
2. Sino-European Institute of Aviation Engineering, Civil Aviation University of China, Tianjin 300300, P. R. China

(Received 18 January 2024; revised 20 April 2024; accepted 8 May 2024)

Abstract: Ingestion of the ice crystals in aircraft engines can lead to the thrust loss or even blade damage, posing a potential threat to flight safety. To investigate the impact characteristics of the ice crystals in the compressor cascade, a method is established to calculate the trajectories of ice crystal particles impacting the blade pressure surface and suction surface separately which can avoid the intersections of the particle trajectories. Based on this method, the effect of the particle size and shape on the ice crystal impact characteristics are numerically studied in details. Results show that the total collection coefficient increases with the increase of the particle equivalent diameter and aspect ratio. For the particles with the same shape, the total collection coefficient increases by 44.1% when the particle diameter increases from 20 μm to 50 μm; for the particles with the same size, the total collection coefficient increases by 39% when the particle aspect ratio increases from 0.1 to 10. The increase of the collection coefficient of the blade pressure surface is the main reason for the increase of the total collection coefficient. The blade leading edge is mainly characterized by the fragmentation of ice crystals and the blade surface is mainly characterized by the rebound of the ice crystals. In most parts of the blade surface, the ice crystal particles have a non-elastic rebound. In terms of the particle size, the distribution trend of the collection coefficient after the secondary impact is very similar to that of the primary impact, with a notable difference being a reduction of about 70% of the maximum value of the collection coefficient. However, in terms of the particle aspect ratio, the trend of the secondary impact collection coefficient at the leading edge of the blade is opposite to that of the primary impact, with elongated ice crystal particles exhibiting a lower secondary collection coefficient.

Key words: ice crystal; compressor cascade; collection coefficient; primary impact; secondary impact

CLC number: V233.94 **Document code:** A **Article ID:** 1005-1120(2024)03-0344-15

0 Introduction

Aircraft icing has long been a crucial factor affecting the flight safety. Previous studies have primarily focused on the aircraft icing induced by the supercooled large droplets (SLD). But since the 1990s, more and more engine thrust loss events have shown that engine icing is also closely related to the ingestion of ice crystals in the high-altitude environment. In 2006, a Qatar Airways Airbus A330 experienced an in-flight shutdown of both engines at an altitude of 6 400 m during the thunderstorm conditions, which was attributed to the ingestion of ice crystals. Likewise, in 2013, a Boeing 747-8 freighter equipped with four GEnx engines experienced ice crystal ingestion at an altitude of approximately 12 km near Chengdu. The ice crystals froze within the engine cores, leading to an in-flight shutdown of the No.2 engine. However, the engine was successfully restarted. The No.1 engine suffered a 70% decrease in rotational speed, which did not fully recover. This is a typical event of ice crystal ingestion of engines resulting in thrust loss and compressor damage[1]. In 2016, a Boeing 787 equipped with GEnx engines experienced an incident of high-altitude ice

---

*Corresponding author, E-mail address: caucjiawei@163.com.

How to cite this article: JIA Wei, GU Yuanhao. Numerical investigation of ice crystal impact characteristics in compressor cascade[J]. Transactions of Nanjing University of Aeronautics and Astronautics, 2024, 41(3): 344-358.

http://dx.doi.org/10.16356/j.1005-1120.2024.03.007

crystal icing. The in-flight shut-down of one engine occurred which could not be restarted. Fortunately, the aircraft landed successfully with only one operated engine.

Ice crystal icing significantly differs from the SLD icing[2]. Ice crystal icing occurs at an average temperature of −36 ℃ and an altitude of approximately 11 km, corresponding to the upper portion of convective cloud layers encountered during the cruising of aircraft. In contrast, SLD icing seldom occurs above 7 km in altitude. The SLD icing commonly occurs in the areas of engine nacelle, inlet guide vanes, and outlet guide vanes, which are usually anti-iced with hot air, electrical heating, or hot oil. However, ice crystal icing mainly occurs within the engine cores. When the ice crystals enter into the compressor, a water film is formed on the blade surface due to the melting of ice crystals. Consequently, the solid ice crystals continuously accumulate on the surfaces, causing icing to occur in the front stages of the low-pressure compressor. Furthermore, visual and radar systems are difficult to detect the ice crystals dispersed at high altitudes. Thus, ice crystal icing imposes more serious challenges to compressor anti-icing. Even if the compressor icing is identified by the pilots, it is difficult to take effective de-icing measures. Therefore, the danger posed by ice crystal icing is much greater than that by SLD icing.

Generally speaking, there are two main differences between the ice crystals and SLD. Firstly, irregular shapes of the ice crystal particles lead to different resistance characteristics and heat transfer characteristics of particles with different shapes. Secondly, when the ice crystals hit the blade surface, the ice crystals will be broken, rebounded or even a secondary impact. The resistance characteristics and heat transfer characteristics of the ice crystals are closely related to the particle shape, and directly affect the trajectory and collection coefficient of the ice crystals. Haider et al.[3], Ganser[4], and Hölzer et al.[5] have proposed different drag models for ice crystal particles. The heat transfer characteristics for non-spherical ice crystal particles in free flow was studied and the heat transfer model for ice crystals has been proposed and developed[6-8]. Besides, Norde et al.[9] computed the trajectory of ice crystals in turbofan engines using both Eulerian and Lagrangian approach and developed an ice accretion method for glaciated as well as mixed-phase icing conditions in turbofan engines. The effects of heat transfer and phase change on the particle trajectory and the impact on the icing surface were considered. Villedieu et al.[10] developed the ONERA 2D toolkit and considered the effect of ice crystal sphericity on the ice crystal phase change and trajectory. The phase change, adhesion, erosion, and icing processes are the key issues in ice crystal icing simulation. It is found that the ice crystal particle adhesion coefficient is positively correlated with liquid film thickness and negatively correlated with the normal kinetic energy recovery coefficient. The NASA-NRC test result was also used to validate the numerical result.

The dynamics of particle-wall interactions following the particle impact are complicated and needed to be carefully considered. At present, the research on the interactions between the SLD and solid wall has been studied widely. After the impact of SLD, some water droplets will splash or rebound, and the secondary droplets will be injected into the flow field again. Four possible mechanisms for SLD-wall interaction were identified by Bai et al.[11]: Adhesion, rebound, spreading and splashing. The mechanisms for ice crystal particle-wall interaction are similar to SLD but have some distinctions. An impact model for ice crystals was proposed by Trontin et al.[12], defining three distinct impact modes: Adhesion, rebound, and fragmentation. During the impact of ice crystal, the particles can either fully adhere to or detach from the surface, maintaining the same size and shape but different velocities. In the fragmentation region, some particles are re-injected into the flow while others remain on the surface. Zhang et al.[13] developed an ice crystal impact model including ice crystal breakup, rebound, and splash on water film. The icing of the NACA0012 under different total water content (TWC) and ice water content (IWC) conditions were simulated. The ice mass and ice shape were compared with experimental result. Norde et al.[8] and Nilamdeen et al.[14] calculated the ice crystal icing process of NACA0012 using the Eulerian approach and both were compared with the experimental results.

In conclusion, it is evident that current studies mainly focus on developing the empirical models to describe the dynamics and thermodynamics of the ice crystal. Moreover, much of the research has concentrated on the airfoil, with relatively few studies on compressor blades. In this paper, a method to simulate the impact characteristic of ice crystals was developed and the impact characteristic of ice crystals within the compressor cascade was investigated.

1 Numerical Method and Validation

All simulations in this paper were performed by ANSYS FLUENT to solve two-dimensional steady Reynolds-averaged Navier-Stokes equations. The SIMPLE algorithm with a pressure-based solver and standard $k-\varepsilon$ turbulence model with standard wall function were adopted to solve the flow field. The Eulerian approach was used to solve the motion of the ice crystal particle. The mass conservation equation, motion equation and the energy equation of the ice crystals were solved using FLUENT UDS after the flow field was converged. Three different UDS equations including the mass conservation equation, the momentum equations and energy equations in two directions need to be solved to simulate the ice crystal impact characteristics. Space was discretized by the second-order upwind scheme. The drag model for non-spherical ice crystals was considered and the method for simulation of the ice crystal secondary impact was also introduced.

1.1 Description of ice crystal geometry

Ice crystals exist in a variety of shapes, including spherical, cylindrical, disk, and hexagonal prisms. The particle sphericity Φ was used to describe the geometrical shape of ice crystals. The particle sphericity is a measure of how close the particle shape approaches that of a sphere with $\Phi=1.0$. Sphericity is defined as the ratio of the surface area A_p of a sphere with the same volume as the particle and the surface area A of that particle which can be expressed as

$$\Phi=\frac{A_p}{A} \tag{1}$$

The diameter of a sphere which has the same volume as the actual is referred to as the particle equivalent diameter d_p.

For axially symmetric particles, such as spheres, cylinders or discs, another geometrical shape descriptor that was widely used in the literature is the aspect ratio. As illustrated in Fig.1, aspect ratio is defined as the ratio of the axial length b of the ice crystal along the rotation axis to the radial length a perpendicular to the rotation axis which can be expressed as

$$E=\frac{b}{a} \tag{2}$$

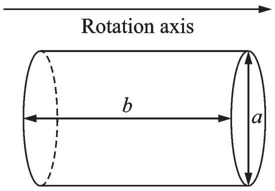

Fig.1 Definition of a and b of the cylindrical ice crystal

Based on the definition of sphericity, an expression can be derived that relates the sphericity of cylindrical ice crystals Φ_c to the aspect ratio E, shown as

$$\Phi_c=\left(\frac{3E}{2}\right)^{1/3}\frac{2}{1+2E} \tag{3}$$

1.2 Ice crystal drag model

In the Eulerian approach, the governing equations for the ice crystals can be expressed as

$$\frac{\partial\alpha}{\partial t}+\nabla\cdot(\alpha\boldsymbol{u})=0 \tag{4}$$

$$\frac{\partial\alpha\boldsymbol{u}}{\partial t}+\nabla\cdot(\alpha\boldsymbol{u}\boldsymbol{u})=\frac{3\boldsymbol{u}_{\mathrm{a}}C_{\mathrm{D}}(Re_{\mathrm{p}},\Phi)Re_{\mathrm{p}}}{4\rho_{\mathrm{p}}d_{\mathrm{p}}^2}\alpha(\boldsymbol{u}_{\mathrm{a}}-\boldsymbol{u})+\alpha\boldsymbol{g} \tag{5}$$

where C_{D} denotes the drag coefficient of ice crystal particles; $\boldsymbol{u}$ the velocity of the ice crystals; $\boldsymbol{u}_{\mathrm{a}}$ the velocity of the air; $\boldsymbol{g}$ the gravitational acceleration; and Re_{p} the relative Reynolds number of the ice crystal particles which can be expressed as

$$Re_{\mathrm{p}}=\frac{\rho_{\mathrm{a}}|\boldsymbol{u}_{\mathrm{a}}-\boldsymbol{u}_{\mathrm{p}}|d_{\mathrm{p}}}{\boldsymbol{u}_{\mathrm{a}}} \tag{6}$$

Different drag coefficient formulas that account for various influencing factors have been proposed[3-5]. By comparing these formulas with the experimental data, Ganser's drag coefficient formula, considering the particle orientation, demonstrates higher accuracy in simulating the drag coefficient of irregular particles, shown as

$$C_{\mathrm{D}}=\frac{24}{Re_{\mathrm{p}}K_1}\cdot\left[1+0.1118\left(Re_{\mathrm{p}}K_1K_2\right)^{0.6567}\right] \tag{7}$$

$$K_1=\left(\frac{1}{3}+\frac{2}{3}\Phi^{-1/2}\right)^{-1} \tag{8}$$

$$K_2=10^{1.8148(-\lg\Phi)^{0.5743}} \tag{9}$$

where the Stokes shape factor K_1 and the Newton shape factor K_2 are both associated with the sphericity of the particles.

The ice crystal local collection coefficient β and the ice crystal total collection coefficient β_{total} are defined as

$$\beta=\frac{\alpha_i\rho_i\boldsymbol{u}\cdot\boldsymbol{n}}{\mathrm{TWC}|\boldsymbol{u}_{\infty}|} \tag{10}$$

$$\beta_{\mathrm{total}}=\int_{s/c}\beta \tag{11}$$

where TWC denotes the total water content measured in $\mathrm{g/m^3}$; $\boldsymbol{n}$ the normal vector to the wall; and $\boldsymbol{u}_{\infty}$ the incoming flow velocity. The collection coefficient is served as the indicator for estimating the amount of ice accumulated on the airfoil surface due to the impact of the ice crystals.

1.3 Ice crystals impact model

Trontin et al.[12] proposed an impact model that defines three distinct impact modes: Adhesion, rebound, and fragmentation. The ice crystal particles can either completely adhere to the surface or completely rebound, maintaining their original size and shape and only the velocity changes. In the fragmentation region, a portion of the particles is rebounded into the air flow, while another portion stays on the surface.

The impact dynamics are strongly influenced by the kinetic energy (based on the normal velocity) of the particles before impact. Therefore, a dimensionless parameter L is introduced, which can be considered as a modified Weber number representing the ratio of kinetic energy to surface energy, shown as

$$L=\frac{\rho_{\mathrm{p}}d_{\mathrm{p}}\boldsymbol{u}_{\mathrm{n}}^2}{12e_{\sigma}} \tag{12}$$

where $\boldsymbol{u}_{\mathrm{n}}$ denotes the normal component of the velocity and the surface energy e_{σ} is defined as

$$e_{\sigma}(T)=e_{\sigma0}\exp\left[\frac{Q_s}{R}\left(\frac{1}{T}-\frac{1}{T_0}\right)\right] \tag{13}$$

where $e_{\sigma0}$ denotes the reference surface energy; Q_s the activation energy, and R the gas constant. It was assumed that the reference value of surface energy is $e_{\sigma0}=0.12\ \mathrm{J/m^2}$ at $T_0=253$ K and the activation energy Q_s is equal to 48.2 kJ/mol. Impact experiment conducted by Hauk et al.[15] confirmed the existence of two critical values of L, including $L_{c_1}=0.5$ and $L_{c_2}=90$. These two critical values define three distinct impact modes: Elastic rebound, non-elastic rebound and fragmentation which generate the secondary particles with different sizes.

The Eulerian method can only handle one particle size, volume fraction, velocity, and temperature per grid cell, resulting in singularities and computational divergence when the trajectories of ice crystal particles intersect. To address this issue, a secondary particle bin method is introduced to separate the incoming primary particles from the outgoing secondary particles. The mass and momentum are not exchanged between the bins, and particles within each bin share the same physical property. The calculation for the primary particle bin is performed first. After obtaining the data of the primary particles, the calculation for the secondary particles is conducted. The secondary particle bin method utilizes the impact parameters of the primary particles as the inlet conditions for the secondary particles colliding with the wall. In the calculation of secondary particles, the far-field values are set to zero, and the Euler trajectory of the secondary particles is computed. Starting from the maximum particle size, the calculation is performed incrementally downwards, as shown in Fig.2. To save computational resources and simulate fragmentation as accurately as possible, five secondary particle bins are employed in this paper.

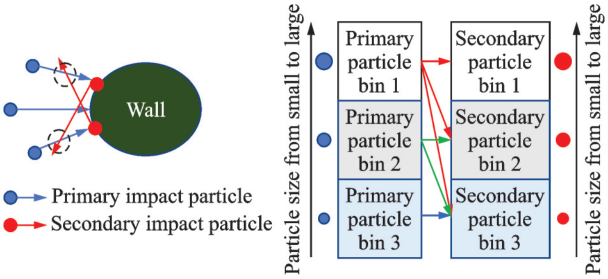

Fig.2 Secondary particle bin method

1.4 Validation

The NACA0012 airfoil with chord $c=1$ m is used to validate the flow field and ice crystal drag model. The computational mesh of NACA0012 airfoil is illustrated in Fig.3. The computational domain is a square region with dimensions of 10 m. The total number of the grid is nearly 36 000.

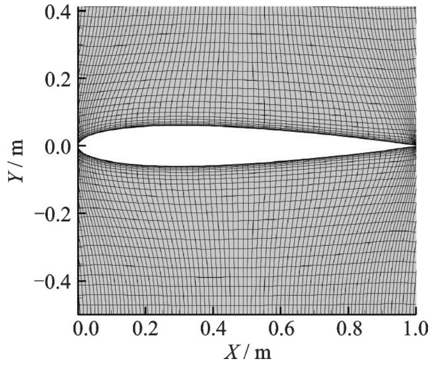

Fig.3 Computational mesh of NACA0012

The experiments conducted by Olayemi et al.[16] is used to verify the flow field solution and the experimental conditions can be found in the literature. The aerodynamic characteristics of NACA0012 are shown in Fig.4. The hollow symbols denote the numerical results and the solid symbols denote the experimental results. The numerical results of aerodynamic characteristics as the drag coefficient C_d ($\times 10^{-2}$) and the lift coefficient C_l of NACA0012 are in good agreement with the experimental results. For the drag coefficient and lift coefficient, the maximum deviations from the experimental results are 2.3% and 3.7%, respectively.

In order to verify the accuracy of the ice crystal drag model, experiments conducted by Wang et al.[17] is referred, the experimental condition can be found in the literature. The collection coefficient is shown in Fig.5, where the horizontal axis represents the Y direction of the airfoil and $Y=0$ denotes the stagnation point of the airfoil. The distribution of the collection coefficient is not symmetric with respect to the line of $Y=0$ because there is a five-degree angle of attack in the experiment. The numerical result shows a good agreement with the experimental result, with a maximum error of only 0.8% in the collection coefficient.

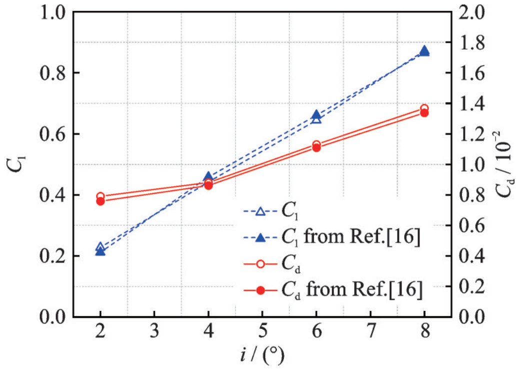

Fig.4 Aerodynamic characteristics of NACA0012

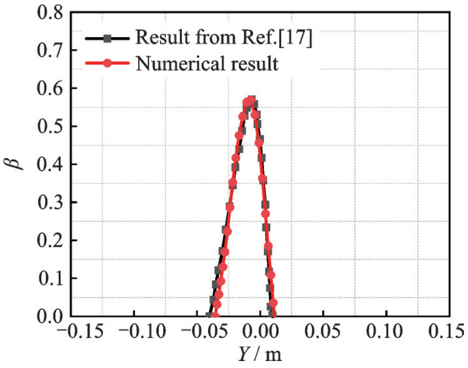

Fig.5 Collection coefficient of NACA0012

The median volume diameter (MVD) is often used to represent the real physical environment and simplify complex distribution for SLD simulation. The same approach is applied to the ice crystals, where the Rosin-Rammler distribution function is used to model the size distribution of the ice crystal particles. A cylinder with $d=1$ m are used to validate the secondary particle bin method. Run #1 to Run #5 represent five different working conditions with $d_p=50$ μm, in which the particle aspect ratio gradually increases, while Run #6 to Run #10 represent five different working conditions with $d_p=200$ μm. The specific conditions can be found in Ref.[2].

In Fig.6, the contours of normalized volume fraction (NVF) after the secondary impact are shown for Run #7 (MVD=200 μm, E=0.7) together with two trajectories in the velocity field of the secondary particles. NVF represents the ratio of the volume fraction of ice crystal particles at any position to the volume fraction of ice crystal particles at the inlet of computational domain. Note that the scale bar is distributed exponentially in the legend. It can be seen that the numerical result in this paper is in good agreement with those in Ref.[2]. Compared with the literature result, the rebound effect is more pronounced near the leading edge of the cylinder and TWC is observed to be slightly higher.

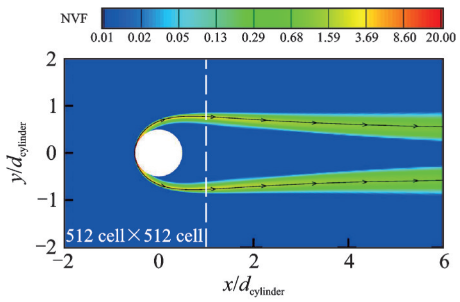

(a) Result from Ref.[2]

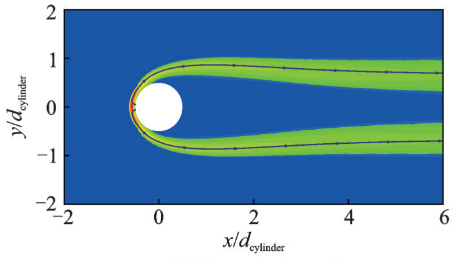

(b) Numerical result

Fig.6 Contours of normalized volume fraction after the secondary impact

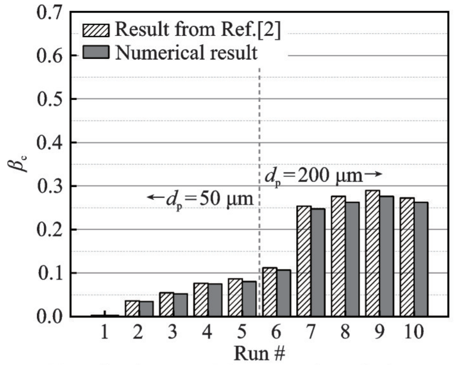

(a) Collection coefficient over the cylinder surface

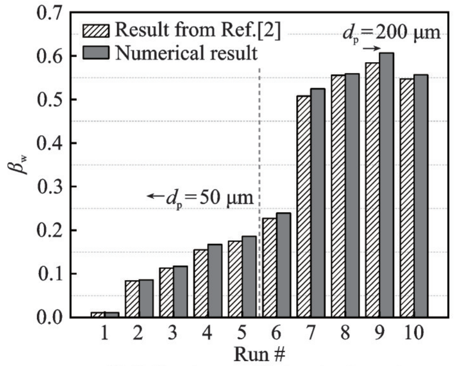

(b) Collection coefficient in the wake

Fig.7 Collection coefficient of the cylinder after the secondary impact

The integral of collection coefficient for MVD=50 μm and MVD=200 μm is shown in Fig.7. To make a clear expression, β_c in Fig.7(a) is defined as the integral over the cylinder surface and β_w in Fig.7(b) is defined as the integral over a vertical traverse from $(x/d,\ y/d)=(1,\ -2)$ to $(x/d,\ y/d)=(1,\ 2)$ indicated by a white dashed line. It should be noted that the collection coefficient in this case is analogous to the total amount of rebounded particles leaving the cylinder surface. For the collection coefficient over the cylinder surface β_c, the average deviation between the numerical result and the literature result is 3.8%. For the collection coefficient in the wake β_w, the average deviation between the numerical result and the literature result is 4%. Therefore, it can be concluded that the numerical method and models employed in this paper are reliable and numerical result is accurate to some extent.

2 Results and Discussion

2.1 Geometry model and computational mesh

A two-dimensional compressor stator cascade originally designed by Duke University[18] was used to analyze the impact characteristics of the ice crystal particles. The cascade has a chord length of 5 cm, an inlet airflow angle of 53.5° and a solidity of 1.25. The computational domain and mesh of the cascade is shown in Fig. 8. The inlet is located at 1.5 times the chord length from the blade leading edge, while the outlet is located at 1.8 times the chord length from the blade trailing edge.

To ensure the mesh independence of the numerical result, four sets of meshes were generated with changing the height of the first layer grid from 1 mm to 0.01 mm. β_m is defined as the maximum

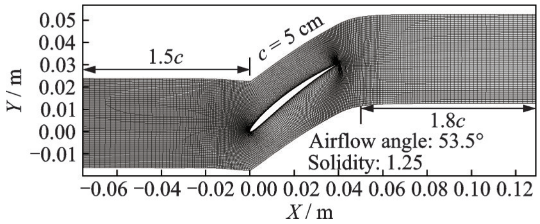

Fig.8 Computational domain and mesh of the compressor cascade

collection coefficient, and σ is defined as the total pressure recovery coefficient. The collection coefficient and total pressure recovery coefficient are shown in Fig.9. The collection coefficient increases by only 0.46% and the change in the total pressure recovery coefficient is only 0.3% as the height of the first layer grid decreased from 0.1 mm to 0.01 mm. Therefore, the height of the first layer grid h was set to 0.1 mm and the total number of the grid was 18 000.

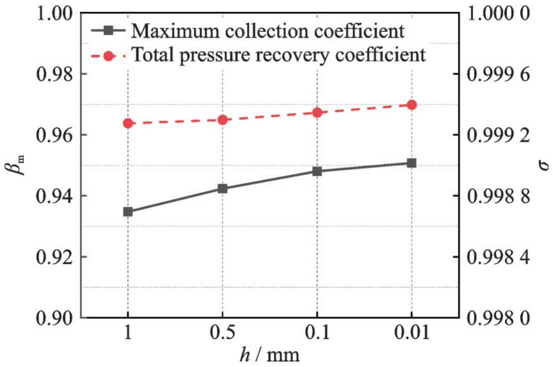

Fig.9 Grid independence result

2.2 Boundary conditions and solving method

All the simulations were performed to solve two-dimensional steady Reynolds-averaged Navier-Stokes equations. The working medium air is an ideal gas. The airflow velocity was imposed at the inlet and the static pressure was imposed at the outlet. The upper boundary and lower boundary were set as periodic boundary conditions, and the blade surface was set adiabatic and non-slip wall. The ambient temperature and pressure of the airflow were 293 K and 101 325 Pa, respectively. The velocity was 60 m/s and the angle of attack of the incoming flow was 0°. The TWC of ice crystal at inlet is 1 g/m^3. The equivalent diameter d_p of the ice crystal particle was 50 μm and the aspect ratio E of ice crystal particle was 0.7. Four parameters describing the distribution of the collection coefficient on the blade surface were selected: The total collection coefficient β_{total}, the maximum collection coefficient at the leading edge $\beta_{\max}$, the maximum collection coefficient at the trailing edge of the pressure surface β_{pressure}, the impact limit on the suction surface $\beta_{\text{suction}[s/c]}$. The previous numerical result showed that due to the small dimension of the blade, the ice crystal particles quickly passed through the blade passage. Consequently, the ice crystal particles did not have sufficient time to melt completely, with the maximum melting rate being less than 0.1%. Therefore, the effect of ice crystal melting can be neglected in this paper. The TWC and IWC are effectively equivalent.

In this simulation, it was assumed that the size of the secondary particles, resulting from the fragmentation of the primary particles, following a Rosin-Rammler distribution. The diameter of the secondary particles was used to calculate the impact characteristic of the ice crystal secondary impact. The periodic boundary conditions of the cascade can cause the trajectories of the ice crystal particles to intersect, resulting in abnormal numerical result. As shown in Fig.10, TWC became exceptionally high in these regions, resulting in local TWC values anomaly and calculation divergence.

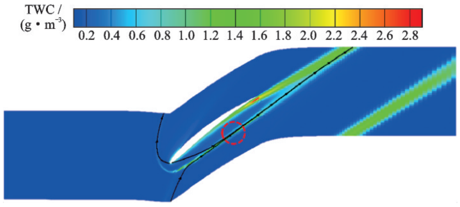

Fig.10 TWC singularity due to periodic boundary conditions

By introducing an additional secondary particle bin, separate calculations were conducted for the pressure and suction surfaces of the blade, effectively preventing the particle trajectory intersection and the anomaly of local parameter. As shown in Fig.11, the particle streamlines displayed here represent the particle trajectories within the individual secondary particle bin.

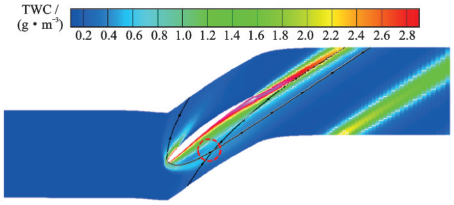

Fig.11 Particle trajectories in the secondary particle bin

2.3 Effect of particle size

In this section, the aspect ratio of the ice crystal particles was set to $E=0.7$. The ice crystal particles with equivalent diameters of $d_p=20$ μm, 30 μm, 40 μm, and 50 μm were considered. The relationship between the total collection coefficient and the ice crystal particle size is shown in Fig.12. As can be seen from Fig.12, the total collection coefficient increases with the increase of particle equivalent diameter. When the particle diameter is increased from 20 μm to 50 μm, the total collection coefficient increases by 44.1%.

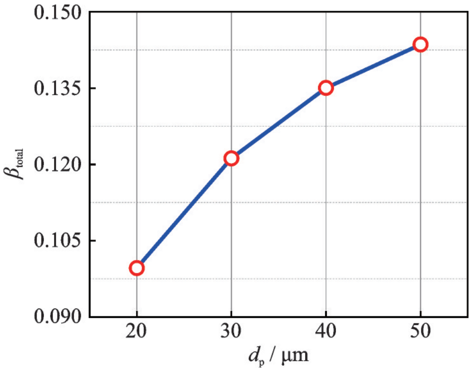

Fig.12 Relationship between total collection coefficient and particle equivalent diameter

The distribution of the collection coefficient along the blade surface for different particle equivalent diameters is shown in Fig.13. In Fig.13, the horizontal axis represents the arc length to chord length ratio (s/c). In the results for the collection coefficient shown in this paper, the curvilinear coordinate was consistently taken from the trailing edge ($s/c=-1$) over the pressure surface of the blade to the leading edge ($s/c=0$) of the blade and back to the trailing edge ($s/c=1$) over the suction surface of the blade. A comparative analysis of the collection coefficient for $d_p=20$ μm and $d_p=50$ μm is given in Table 1. It is apparent that the collection coefficient at the stagnation point of the blade reaches its maximum when ice crystal particles impact on the blade at zero angle of attack. With the increase of the particle size, there is only a limited increase in the maximum collection coefficient. Specifically, as the particle equivalent diameter increases from 20 μm to 50 μm, the maximum collection coefficient increases by only 1.03%.

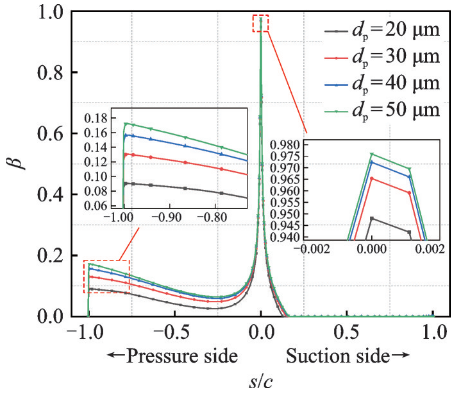

Fig.13 Distribution of collection coefficient for different particle equivalent diameters

Table 1 Collection coefficient for $d_p=20$ μm and $d_p=50$ μm

d_p/μm	β_{total}	β_{max}	$\beta_{pressure}$	$\beta_{suction[s/c]}$
20	0.100	0.972	0.107	0.133
50	0.146	0.982	0.171	0.169

Obviously different from the airfoil, the pressure surface of the compressor cascade is concave while the suction surface is convex. Therefore, the ice crystal particles tend to be accumulated on the blade pressure surface, especially near the blade trailing edge, resulting in a local peak in the collection coefficient. Subsequently, the collection coefficient progressively decreases from the blade trailing edge towards the blade leading edge, before rapidly increasing to its maximum value at the stagnation point. Specifically, as the particle equivalent diameter increases from 20 μm to 50 μm, there is an increase of 59.8% in the maximum collection coefficient of the blade pressure surface.

Due to the convex nature of the blade suction surface, the accumulation of ice crystal particles is more challenging on this surface, leading to a lower collection coefficient of the blade suction surface compared with that on the blade pressure surface. Furthermore, the impact limit on the suction surface is notably lower than that on the pressure surface. With the increase of the particle size, there is a slightly increase in the impact limit on the suction surface. As the particle equivalent diameter increases from 20 μm to 50 μm, the impact limit on the suction surface increases from 0.133 to 0.169 in terms of s/c. Therefore, it can be concluded that the increase of the collection coefficient of the blade pressure surface dominates the increase of the blade total collection coefficient.

With the increase of the equivalent diameter, the mass of the ice crystal increases, resulting in the increase of the inertia force of the ice crystal particles and the decrease of the sensitivity to air flow. Fig.14 shows the contours of TWC for the ice crystal particles with $d_p=20$ μm and $d_p=50$ μm. Most of the ice crystal particles impact on the blade pressure surface and leading edge, while relatively few particles impact on the blade suction surface. The ice crystal particles with larger diameter possesses higher inertia. This means that they are more likely to overcome the influence of the airflow and directly impact on or away from the blade surface. The ice crystal particles with large diameter impacting on the blade surface also result in larger regions with low value of TWC on the rear part of the blade suction surface and in the wake. In contrast, small ice crystal particles are more sensitive to the air flow and follow the airflow around the leading edge before leaving the blade suction surface.

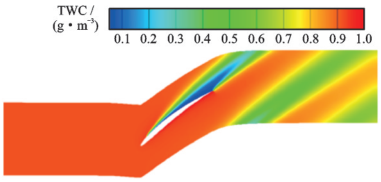

(a) $d_p = 20$ μm

(b) $d_p = 50$ μm

Fig.14 Contours of TWC after the primary impact for $d_p=20$ μm and $d_p=50$ μm

Base on the previous discussion, the equivalent Weber number L for the ice crystals is a critical parameter describing the behavior of ice crystals impacting the wall. It includes two significant thresholds: $L_{c_1}=0.5$ and $L_{c_2}=90$. When $L<L_{c_1}$, the impact is relatively gentle, and the ice crystal undergoes elastic rebound without any loss of momentum. When $L_{c_1}<L<L_{c_2}$, non-elastic rebound occurs, resulting in a loss of momentum, but the ice crystal remains intact with no change in size. When $L>L_{c_2}$, the impact becomes more severe, causing the ice crystal to fragment and generate secondary particles of different sizes. The distribution of L for the ice crystal particles with $d_p = 20$ μm and $d_p = 50$ μm after the primary impact is shown in Fig.15, including Fig.15(a) L over the blade surface, Fig.15(b) region of elastic rebound, Fig.15(c) region of non-elastic rebound, and Fig.15(d) region of fragmentation.

From the perspective of blade shapes, the blade leading edge is relatively sharp which makes it easier for the impact energy to be concentrated in a small area, resulting in fragmentation. In contrast, other positions on the blade surface have larger curvature, making it easier for the ice crystals to rebound. According to the definition of the equivalent Weber number L, at the blade leading edge, the relative velocity of the ice crystals is higher, and the angle between the incoming flow velocity and the blade surface normal vector is relatively small when the ice crystals impact the blade leading edge. Therefore, the fragmentation occurs when L exceeds L_{c_2}.

Similarly, there is a positive correlation between the equivalent Weber number L and particle diameter d_p. In most regions of the blade pressure surface, the ice crystal particles have a non-elastic rebound, resulting in a loss of momentum with a constant particle diameter. There is an elastic rebound region on the blade pressure surface for $d_p=20$ μm. With the increase of the particle size, the region of elastic rebound on the blade pressure surface disappears. Meanwhile, there is a significant in-

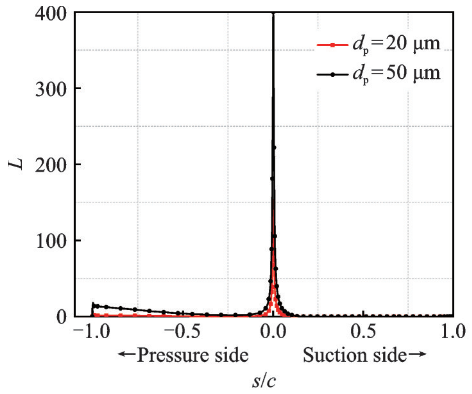

(a) Global distribution over the blade surface

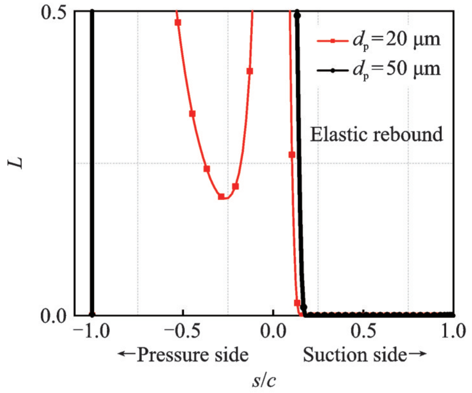

(b) Region of elastic rebound

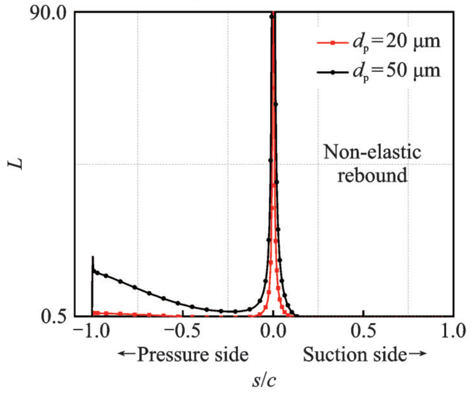

(c) Region of non-elastic rebound

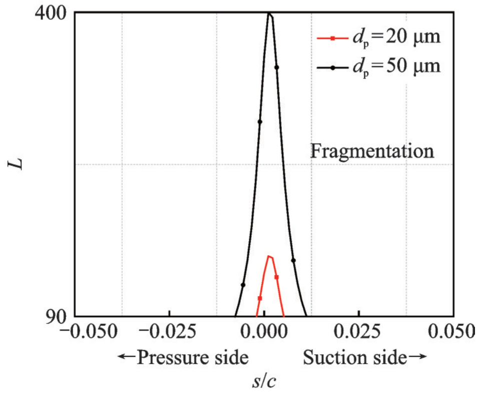

(d) Region of fragmentation

Fig.15 Distribution of equivalent Weber number for d_p=20 μm and d_p=50 μm

crease in the extent of non-elastic rebound and fragmentation. The fragmentation region in terms of s/c for $d_p=50$ μm is from -0.008 to 0.012, compared with that of $d_p=20$ μm is from -0.002 to 0.005. The peak value of L for $d_p=50$ μm is 2.6 times higher than that of $d_p=20$ μm.

The distribution of the collection coefficient for different particle equivalent diameters after the secondary impact is shown in Fig.16. For clarity, β_2 denotes the collection coefficient after the secondary impact. The definition of the secondary impact collection coefficient only focuses on the ice crystal particles that hit the blade and subsequently rebounded or fragmented. These particles are carried by the airflow for a secondary impact on the blade surface again. The distribution trend of the collection coefficient after the secondary impact is very similar to that of the primary impact, with a notable difference being a reduction of about 70% of the maximum value of the collection coefficient.

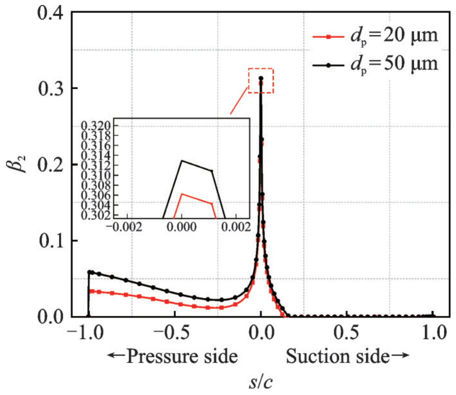

Fig.16 Distribution of collection coefficient after the secondary impact for d_p=20 μm and d_p=50 μm

Fig.17 shows the contours of TWC for the ice crystal particles with $d_p=20$ μm and $d_p=50$ μm after the secondary impact. It can be observed that the local peak of TWC appears near the trailing edge of the blade pressure surface. This suggests that the ice crystal particles are more likely to accumulate near the blade trailing edge. After impacting the blade surface, the ice crystal particles fragment and bounce away from the blade as indicated by the red dashed line. Then the movement direction of the ice crystal particles is changed by the airflow. Subsequently, the ice crystal particles move towards the blade and are collected near the blade trailing edge.

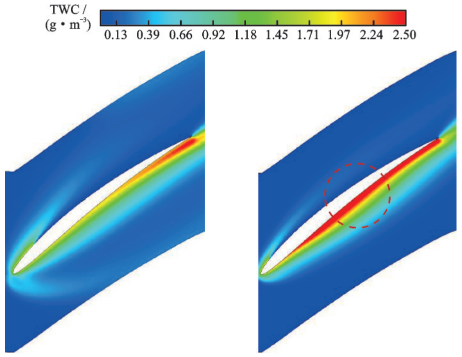

(a) $d_p = 20$ μm (b) $d_p = 50$ μm

Fig.17 Contours of TWC after the secondary impact for d_p=20 μm and d_p=50 μm

2.4 Effect of particle shape

In this section, the equivalent diameter of the ice crystal particles is set to d_p=50 μm. The ice crystal particles with aspect ratios of E=0.1, 0.7, 1, 5 and 10 are considered. Assuming that the shape of the non-spherical ice crystal particles is cylindrical, the aspect ratio E is used to characterize the shape of ice crystal particles. Here, E<1 indicates that the ice crystal particles are short and thick in the direction of motion, while E>1 indicates that the particles are elongated.

The relationship between the total collection coefficient and the ice crystal particle aspect ratio is shown in Fig.18. As can be seen from Fig.18, the collection coefficient is changed due to different particle shapes and the total collection coefficient increases with the increase of particle aspect ratio. When the particle aspect ratio is increased from 0.1 to 10, the total collection coefficient increases by 39%. The reason for the higher collection coefficient of elongated ice crystals can be attributed to the fact that the elongated ice crystal particles are more likely to move along the direction of the flow.

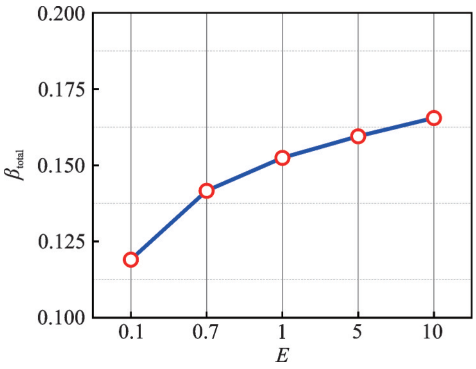

Fig.18 Relationship between total collection coefficient and particle aspect ratio

The distribution of the collection coefficient along the blade surface for different particle aspect ratios is shown in Fig.19. A comparative analysis of the collection coefficient for E=0.1 and E=10 is shown in Table 2. The reason for the increase in the total collection coefficient for different shapes is mainly due to the increase of collection coefficient of the blade pressure surface. The collection coefficient of the blade pressure surface increases with the increase of particle aspect ratio. For the ice crystal particle with E=10, the maximum collection coefficient on the blade pressure surface increases by 64.4% compared with that of E=0.1. The elongated shape of the ice crystal particle allows them to effectively follow the airflow and thus makes them more likely to follow the airflow directly to the pressure surface. As the particle aspect ratio increases from 0.1 to 10, the collection coefficient nearly remains unchanged but the impact limit increases from 0.160 to 0.179 in terms of s/c, indicating a broader impact region.

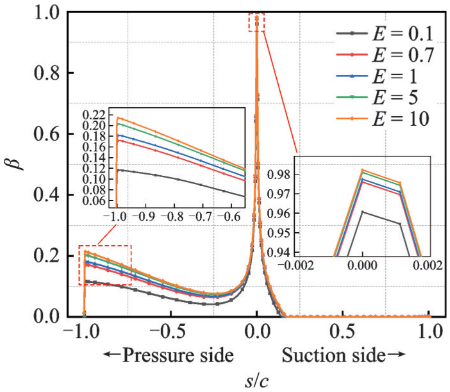

Fig.19 Distribution of collection coefficient for different particle aspect ratios

Table 2 Collection coefficient for E=0.1 and E=10

E	β_{total}	β_{max}	$\beta_{pressure}$	$\beta_{suction[s/c]}$
0.1	0.119	0.965	0.132	0.160
10	0.166	0.983	0.217	0.179

Fig.20 shows the contours of TWC for the ice crystal particles with E=0.1 and E=10. When the particle aspect ratio increases from 0.1 to 10, the low TWC region near the blade suction surface changes little. However, the value of TWC in the wake is noticeably decreases. Compared with the effect of the particle size discussed above, the particle aspect ratio has a less significant effect on the TWC near the blade suction surface.

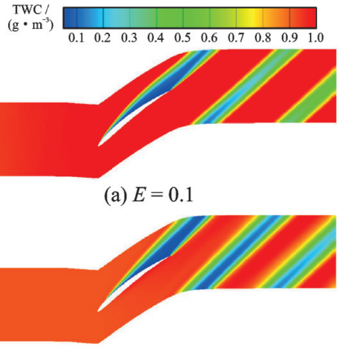

(a) $E = 0.1$

(b) $E = 10$

Fig.20 Contours of TWC after the primary impact for $E=0.1$ and $E=10$

The distribution of L for the ice crystal particles with $E=0.1$ and $E=10$ after the primary impact is shown in Fig.21. Ice crystals with elongated shapes exhibit more stable motion in the air due to their streamlined shape. For this kind of ice crystals, there is a smaller angle between the incoming flow and the blade surface normal vector, resulting in a larger u_n. In contrast, ice crystals with a short and thick shape may be more susceptible to the influence of airflow, leading to more unstable motion and a smaller u_n. For the same equivalent diameter, ice crystal with elongated shapes exhibit larger equivalent Weber number compared with that of the short and thick particles. Additionally, when impacting a surface, the smaller contact area of elongated ice crystals concentrates the impact force, resulting in more intense impacts and higher pressure at the impact point.

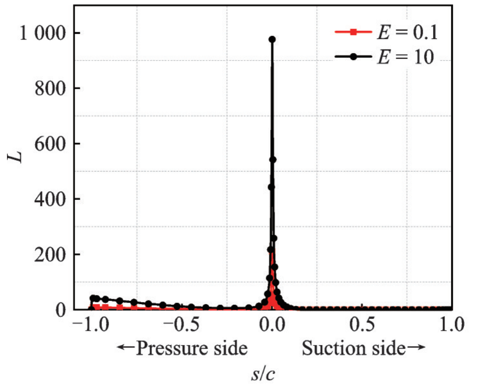

(a) Global distribution over the blade surface

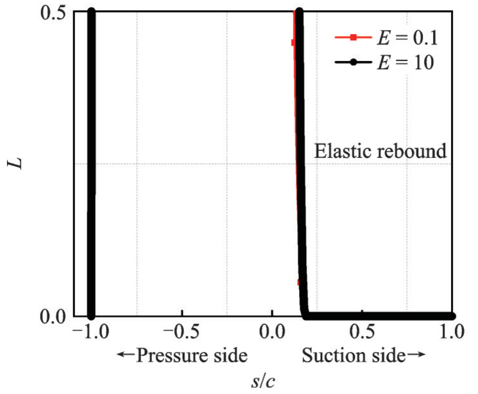

(b) Region of elastic rebound

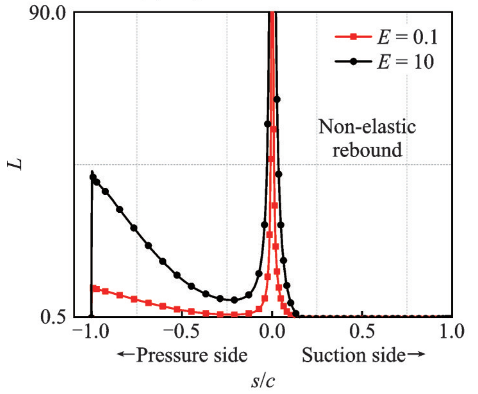

(c) Region of non-elastic rebound

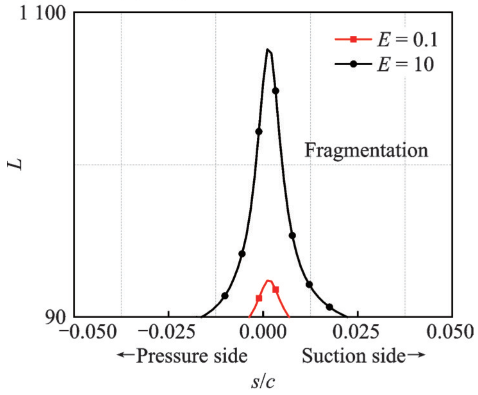

(d) Region of fragmentation

Fig.21 Distribution of equivalent Weber number for $E=0.1$ and $E=10$

There is almost no elastic rebound on the blade pressure surface. However, elastic rebound exits near the impact limit of the blade suction surface. The fragmentation region in term of s/c is from -0.018 to 0.022 for $E=10$ while from -0.004 to 0.008 for $E=0.1$. The peak value of L for $E=10$ is 4.6 times higher than that of $E=0.1$. For the elongated ice crystal particles, when impacting on the blade leading edge, the impact force may concentrates on a smaller area, leading to higher pressure at the impact position and higher intensity of the impact. In contrast, the impact force of the short and thick ice crystal particles may be distributed over a larger area, reducing the intensity of the impact.

The distribution of the collection coefficient for different particle aspect ratios after the secondary impact is shown in Fig.22. The result shows that in most regions of the blade suction and pressure surfaces, the distribution trend of the collection coefficient after the secondary impact is basically consistent with that of the primary impact, that is the elongated ice crystal particles demonstrating higher collection coefficient compared with the short and thick ice crystal particles. However, there is an opposite trend at the blade leading edge, where the elongated ice crystal particles exhibit a lower secondary collection coefficient. This is because the elongated ice crystals are more prone to break and rebound after impacting the blade. In contrast, the short and thick ice crystal particles possess a more stable structure, which enable them to remain intact more easily during impact, thus resulting in a higher collection coefficient at the blade leading edge.

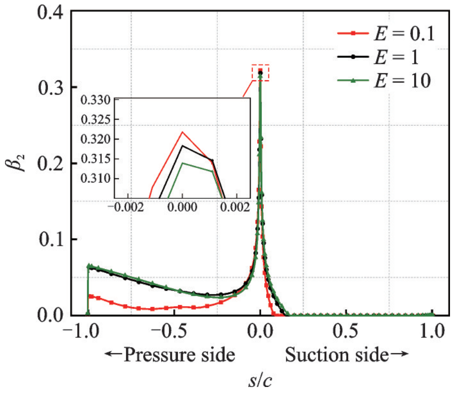

Fig.22 Distribution of collection coefficient after the secondary impact for $E=0.1$ and $E=10$

Fig.23 shows the contours of TWC for the ice crystal particles with $E=0.1$ and $E=10$ after the secondary impact. For the ice crystal particles with $E=0.1$, the particles are dispersed into the surroundings and subsequently guided by the airflow after impacting the blade. Due to the poor sensitivity to the airflow, a greater number of particles travel further away from the blade pressure surface and consequently are accumulated near the trailing edge of the blade pressure surface. However, for the ice crystal particles with $E=10$, the particles are more easily transported by the airflow to the blade pressure surface after impacting the blade as indicated by the red dashed line. This allows the ice crystal particles to accumulate on the blade pressure surface earlier. Therefore, the value of TWC is relatively high from the front part to the trailing edge of the blade pressure surface.

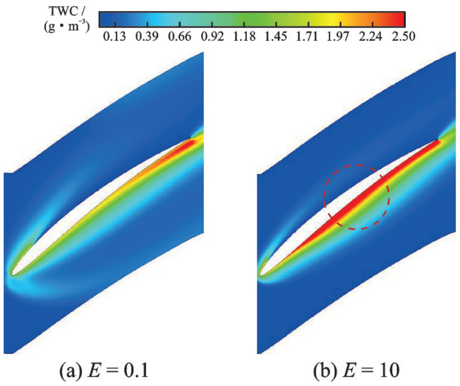

(a) $E = 0.1$ (b) $E = 10$

Fig.23 Contours of TWC after the secondary impact for $E=0.1$ and $E=10$

3 Conclusions

A new method to simulate the secondary impact characteristics of ice crystals is established. The impact characteristics of ice crystal particles in a typical compressor stator cascade is investigated numerically. The main conclusions can be drawn as follows:

(1) The total collection coefficient increases with the increase of particle equivalent diameter. When the particle diameter is increased from 20 μm to 50 μm, the total collection coefficient increases by 44.1%. The increase of the collection coefficient of the blade pressure surface dominates the increase of the blade total collection coefficient. As the particle equivalent diameter increases from 20 μm to 50 μm, there is an increase of 59.8% in the maximum collection coefficient of the blade pressure surface.

(2) The blade leading edge is mainly characterized by the fragmentation of ice crystals and the blade surface is mainly characterized by the rebound of the ice crystals. In most parts of the blade pressure surface, the ice crystal particles have a non-

elastic rebound. There is an elastic rebound region on the blade pressure surface for $d_p=20$ μm, while for $d_p=50$ μm the region of elastic rebound on the blade pressure surface disappears. In terms of the particle size, the distribution trend of the collection coefficient after the secondary impact is very similar to that of the primary impact, with a notable difference being a reduction of about 70% of the maximum value of the collection coefficient.

(3) The total collection coefficient increases with the increase of particle aspect ratio. When the aspect ratio is increased from 0.1 to 10, the total collection coefficient increases by 39%. For the ice crystal particles with $E=10$, the maximum collection coefficient on the blade pressure surface increases by 64.4% compared with that of $E=0.1$. There is a noticeable expansion of the fragmentation region for the ice crystal particles with $E=10$. The peak value of equivalent Weber number for the ice crystal particles with $E=10$ is 4.6 times higher than that of the ice crystal particles with $E=0.1$.

(4) In terms of the particle aspect ratio, the trend of the secondary impact collection coefficient at the leading edge of the blade is opposite to that of the primary impact, with elongated ice crystal particles exhibiting a lower secondary collection coefficient. For the ice crystal particles with $E=0.1$, the secondary particles accumulated only near the trailing edge of the blade pressure surface. However, for the ice crystal particles $E=10$, the secondary particles accumulated on the most parts of the blade pressure surface.

References

[1] KHAROUFAH H, MURRAY J, BAXTER G, et al. A review of human factors causations in commercial air transport accidents and incidents: From to 2000—2016[J]. Progress in Aerospace Sciences, 2018, 99: 1-13.

[2] NORDE E. Eulerian method for ice crystal icing in turbofan engines[D]. Enschede, The Netherlands: University of Twente, 2017.

[3] HAIDER A, LEVENSPIEL O. Drag coefficient and terminal velocity of spherical and nonspherical particles[J]. Powder Technology, 1989, 58(1): 63-70.

[4] GANSER G H. A rational approach to drag prediction of spherical and nonspherical particles[J]. Powder Technology, 1993, 77(2): 143-152.

[5] HÖLZER A, SOMMERFELD M. New simple correlation formula for the drag coefficient of non-spherical particles[J]. Powder Technology, 2008, 184(3): 361-365.

[6] IULIANO E, MONTREUIL E, NORDE E, et al. Modelling of non-spherical particle evolution for ice crystals simulation with an eulerian approach[C]//Proceedings of SAE 2015 International Conference on Icing of Aircraft, Engines, and Structures. [S.l.]: SAE, 2015: 2138.

[7] TRONTIN P, VILLEDIEU P. A comprehensive accretion model for glaciated icing conditions[J]. International Journal of Multiphase Flow, 2018, 108: 105-123.

[8] NORDE E, VAN DER WEIDE E T A, HOEIJMAKERS H W M. Eulerian method for ice crystal icing[J]. AIAA Journal, 2018, 56(1): 222-234.

[9] NORDE E, SENONER J M, VAN DER WEIDE E T A, et al. Eulerian and lagrangian ice-crystal trajectory simulations in a generic turbofan compressor[J]. Journal of Propulsion and Power, 2019, 35(1): 26-40.

[10] VILLEDIEU P, TRONTIN P, CHAUVIN R. Glaciated and mixed phase ice accretion modeling using ONERA 2D icing suite[C]//Proceedings of the 6th AIAA Atmospheric and Space Environments Conference. Atlanta, USA: AIAA, 2014.

[11] BAI C, GOSMAN A D. Development of methodology for spray impingement simulation[C]//Proceedings of International Congress & Exposition. [S.l.]: SAE, 1995: 950283.

[12] TRONTIN P, BLANCHARD G, VILLEDIEU P. A comprehensive numerical model for mixed-phase and glaciated icing conditions[C]//Proceedings of the 8th AIAA Atmospheric and Space Environments Conference. Washington, DC, USA: AIAA, 2016.

[13] ZHANG L, LIU Z, ZHANG M. Numerical simulation of ice accretion under mixed-phase conditions[J]. Proceedings of the Institution of Mechanical Engineers, Part G: Journal of Aerospace Engineering, 2016, 230(13): 2473-2483.

[14] NILAMDEEN S, HABASHI W, AUBÉ M, et al. FENSAP-ICE: Modeling of water droplets and ice crystals[C]//Proceedings of the 1st AIAA Atmospheric and Space Environments Conference. San Antonio, USA: AIAA, 2009.

[15] HAUK T, BONACCURSO E, VILLEDIEU P, et

al. Theoretical and experimental investigation of the melting process of ice particles[J]. Journal of Thermophysics and Heat Transfer, 2016, 30(4): 946-954.

[16] OLAYEMI O A, OGUNWOYE O V, OLABEMIWO J T, et al. Analysis of flow characteristics around an inclined NACA0012 airfoil using various turbulence models[J]. IOP Conference Series: Materials Science and Engineering, 2021, 1107(1): 012133.

[17] WANG Z, LIU C, ZHONG W, et al. Numerical simulation of ice crystal trajectory and its influencing factors based on lagrangian method[J]. Applied Sciences, 2023, 13(7): 4110.

[18] EKICI K, HALL K C. Nonlinear analysis of unsteady flows in multistage turbomachines using harmonic balance[J]. AIAA Journal, 2007, 45(5): 1047-1057.

Acknowledgement This work was supported by the Fundamental Research Funds for the Central Universities (No. 3122025101).

Author Prof. **JIA Wei** received the B.E. and Ph.D. degrees in fluid machinery and engineering from Beijing University of Aeronautics and Astronautics, Beijing, China, in 2008 and 2014, respectively. From 2014 to present, he has been with the College of Safety Science and Engineering, Civil Aviation University of China (CAUC). His research has focused on aero engine ice crystal/ mixed-phase icing mechanism and numerical simulation method.

Author contributions Prof. **JIA Wei** contributed to the discussion and background of the study, designed the study, conducted the analysis, interpreted the results and wrote the manuscript. Mr. **GU Yuanhao** complied the models and contributed to data. All authors commented on the manuscript draft and approved the submission.

Competing interests The authors declare no competing interests.

(Production Editor: ZHANG Bei)

压气机叶栅冰晶撞击特性的数值模拟研究

贾 惟[1]，顾元昊[2]

（1.中国民航大学安全科学与工程学院，天津 300300，中国；
2.中国民航大学中欧航空工程师学院，天津 300300，中国）

摘要：航空发动机吸入冰晶会导致推力损失甚至叶片损坏，对飞行安全构成潜在威胁。为了研究冰晶在压气机叶栅中的撞击特性，建立了一种分别计算颗粒撞击叶片压力面和吸力面时运动轨迹的方法，该方法可以避免冰晶颗粒轨迹交叉。在此基础上，对颗粒等效直径和形状对冰晶撞击特性的影响进行了数值模拟研究。结果表明，总收集系数随颗粒等效直径和长宽比的增加而增加。对于相同形状的颗粒，当颗粒直径从 20 μm 增加到 50 μm 时，总收集系数增加了 44.1%；对于相同等效直径的颗粒，当颗粒长宽比从 0.1 增加到 10 时，总收集系数增加了 39%。叶片压力面收集系数的增加是总收集系数增加的主要原因。冰晶撞击叶片前缘时发生破碎现象，撞击叶片表面时发生反弹现象。在叶片表面的大部分区域，冰晶颗粒发生非弹性反弹。就粒径而言，二次撞击后收集系数的分布趋势与一次撞击近似，二次收集系数的最大值减少了约 70%。然而，就颗粒长宽比而言，叶片前缘处二次撞击收集系数的分布趋势与一次撞击相反，细长型冰晶颗粒撞击叶片前缘的二次收集系数反而低于粗短型冰晶颗粒撞击叶片前缘的二次收集系数。

关键词：冰晶；压气机叶栅；收集系数；一次撞击；二次撞击